# Extremely large magnetoresistance and anisotropic transport in the multipolar Kondo system $PrTi_2Al_{20}$

Takachika Isomae,[1] Akito Sakai,[2] Mingxuan Fu,[1,2] Takanori Taniguchi,[3] Masashi Takigawa,[1,4,5] and Satoru Nakatsuji[1,2,6,7,8,*]

[1]*Institute for Solid State Physics, University of Tokyo, Kashiwa, Chiba 277-8581, Japan*
[2]*Department of Physics, Faculty of Science and Graduate School of Science, The University of Tokyo, Hongo, Bunkyo-ku, Tokyo 113-0033, Japan*
[3]*Institute for Materials Research, Tohoku University, Sendai, Miyagi 980-8577, Japan*
[4]*Institute of Materials Structure Science, High Energy Accelerator Research Organization (KEK-IMSS), Oho, Tsukuba, Ibaraki 305-0801, Japan*
[5]*Toyota Physical and Chemical Research Institute, Nagakute, Aichi 480-1192, Japan*
[6]*CREST, Japan Science and Technology Agency (JST), 4-1-8 Honcho Kawaguchi, Saitama 332-0012, Japan*
[7]*Institute for Quantum Matter and Department of Physics and Astronomy, Johns Hopkins University, Baltimore, Maryland 21218, USA*
[8]*Trans-scale Quantum Science Institute, University of Tokyo, Bunkyo-ku, Tokyo 113-0033, Japan*

(Received 13 October 2022; revised 17 May 2023; accepted 18 August 2023; published 3 January 2024)

Multipolar Kondo systems offer unprecedented opportunities to design astonishing quantum phases and functionalities beyond spin-only descriptions. A model material platform of this kind is the cubic heavy fermion system $PrT_2Al_{20}$ ($T$ = Ti, V), which hosts a nonmagnetic crystal-electric-field ground state and substantial Kondo entanglement of the local quadrupolar and octopolar moments with the conduction electron sea. Here, we explore the magnetoresistance (MR) and Hall effect of $PrTi_2Al_{20}$, which develops ferroquadrupolar (FQ) order below $T_Q \sim 2$ K, and compare their behavior with that of the MR and Hall effect of the non-4$f$ analog, $LaTi_2Al_{20}$. In the FQ ordered phase, $PrTi_2Al_{20}$ displays extremely large magnetoresistance (XMR) of $\sim 10^3\%$. The unsaturated, quasilinear field ($B$) dependence of the XMR violates Kohler's scaling and defies description based on carrier compensation alone. By comparing the MR and the Hall effect observed in $PrTi_2Al_{20}$ and $LaTi_2Al_{20}$, we conclude that the open-orbit topology on the electron-type Fermi surface sheet is key for the observed XMR. The low-temperature MR and the Hall resistivity in $PrTi_2Al_{20}$ display pronounced anisotropy in the [111] and [001] magnetic fields, which is absent in $LaTi_2Al_{20}$, suggesting that the transport anisotropy ties in with the anisotropic magnetic field response of the quadrupolar order parameter.

DOI: 10.1103/PhysRevResearch.6.013009

## I. INTRODUCTION

The quest for material platforms exhibiting large magneto-transport has pushed progress in both fundamental science and technological applications. The outstanding examples, such as giant magnetoresistance in magnetic multilayers, are typically engendered by the interplay of the spin structure with charge transport [1,2]. Recent studies have uncovered extremely large magnetoresistance (XMR) in nonmagnetic metals and semimetals, some featuring novel topological band structure, such as Dirac or Weyl nodes [3–10]. Nevertheless, a universal understanding of the mechanism behind the observed XMR is lacking. Aside from the spin and charge degrees of freedom, electron orbitals are a critical ingredient for creating new quantum phases and functionalities in strongly correlated systems [11–13]. Since the electronic band structure finds its root in the interplay between orbitals and the crystal lattice, the ordering and fluctuations of orbitals are expected to yield remarkable effects on transport properties. In 3$d$ transition metal compounds, however, the spin, orbital, and charge degrees of freedom are inextricably intertwined, thus hindering a clear understanding of how orbital ordering and fluctuations tie in with novel transport phenomena. In contrast, cubic 4$f$ rare-earth materials may host a nonmagnetic crystal-electric-field (CEF) ground state with high-rank multipolar moments, offering a route to materialize novel transport phenomena of a purely orbital origin [14–17].

The multipolar Kondo system $PrTi_2Al_{20}$ provides a suitable stage for investigating orbital ordering and its ties to exotic electronic transport. In this system, the cubic $T_d$ symmetry of the Pr site stabilizes a non-Kramers $\Gamma_3$ doublet ground state that carries quadrupolar and octupolar, but no magnetic dipolar moments [18]. This nonmagnetic ground-state doublet is well separated from the first-excited magnetic triplet by a CEF gap of $\Delta_{CEF} \sim 60$ K and thus governs the low-temperature properties of the system [18–20]. A

*Corresponding author: satoru@phys.s.u-tokyo.ac.jp

ferroquadrupolar (FQ) order with the order parameter $O_{20}$ ($3J_x^2 - J^2$, $3J_y^2 - J^2$, and $3J_z^2 - J^2$) develops below $T_Q \sim 2$ K at zero magnetic field [20–22], with a superconducting transition inside the FQ phase [23]. Moreover, the cagelike local structure maximizes the number of Al ions surrounding the Pr $4f$ moments, leading to substantial Kondo entanglement of the multipolar moments with the conduction ($c$) electrons and formation of heavy quasiparticles, as experimentally confirmed by various experimental probes [18,24–27]. Pressure tuning of $PrTi_2Al_{20}$ results in a rich phase diagram featuring strongly enhanced superconducting transition temperature $T_c$ and quasiparticle effective mass $m^*$ on approaching the FQ phase boundary and robust non-Fermi-liquid (NFL) behavior over a wide parameter range [28]. The multipolar Kondo effect and quantum critical fluctuations originating from the orbital degrees of freedom are essential in generating the observed exotic superconductivity and NFL state.

On the other hand, magnetotransport phenomena in $PrTi_2Al_{20}$ have not been explored. A giant anisotropic magnetoresistance ratio (AMR) of about 20% has recently been reported in the sister compound $PrV_2Al_{20}$ under a [001] magnetic field [29], similar to that observed in the nematic order in iron-based superconductors [12]. This AMR is believed to be driven by quadrupolar (i.e., orbital) rearrangement and the accompanied Fermi surface (FS) change [29], which opens intriguing prospects of exotic magnetotransport stemming from the interplay of FS properties with the FQ order in $PrTi_2Al_{20}$. However, investigations into the FS properties of $PrT_2Al_{20}$ ($T$ = Ti, V) are particularly challenging. Density functional theory (DFT) calculation of the FS is obscured by the large number of atoms in one unit cell and the strong electronic correlation. Experimentally, a recent de Haas–van Alphen (dHvA) study on $PrTi_2Al_{20}$ and $LaTi_2Al_{20}$ reveals a complex FS comprising multiple electron and hole sheets in both materials [27]. The resolved FS sheets in $PrTi_2Al_{20}$ show similar geometry to those in $LaTi_2Al_{20}$, while some electron FS sheets in $PrTi_2Al_{20}$ have enhanced cyclotron effective mass $\sim(8–10)m_0$, indicating their sensitivity to the $c$-$f$ hybridization effect [27]. Moreover, nuclear magnetic resonance (NMR) [22], magnetization [22], and specific heat [30] measurements indicate that an applied magnetic field of about 2 T along certain orientations induces a discontinuous switching of the FQ order parameter, likely accompanied by a change in the $c$-$f$ hybridization which may cause the reconstruction of the FS. This possible field-induced FS reconstruction due to changes in FQ ordering structure remains an open question; quantum oscillations are observed only for $B \gtrsim 2$ T, thus offering no evidence for the potential low-field FS changes [27]. MR and the Hall effect are effective alternatives for probing FS properties; comparing their behavior in $PrTi_2Al_{20}$ and $LaTi_2Al_{20}$ may yield more profound insights into the interplay of FS and electrical transport properties with multipolar ordering and fluctuations.

In this paper, we report transverse MR and the Hall effect $\rho_H$ in high-quality single-crystal $PrTi_2Al_{20}$ and its non-$4f$ analog $LaTi_2Al_{20}$. Comparing the observed features for these two materials reveals that open orbits on the electron-type FS sheets are essential for inducing the three-orders-of-magnitude increase of transverse MR across the FQ transition in $PrTi_2Al_{20}$. Moreover, the MR and Hall effect in $PrTi_2Al_{20}$ develop strong anisotropy on approaching the FQ phase, intimately linked to the sharply distinct behavior of quadrupolar order and fluctuations in different magnetic field orientations. The details about the material synthesis and experimental methods are provided in the Appendix.

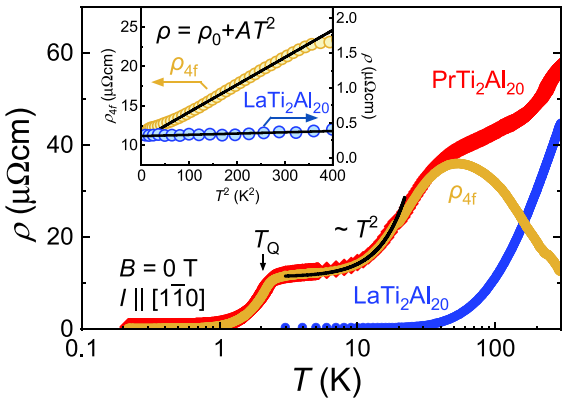


FIG. 1. Temperature $T$ dependence of the zero-field resistivity $\rho$ for $PrTi_2Al_{20}$ (solid red circles) and $LaTi_2Al_{20}$ (solid blue circles). The $4f$-electron contribution $\rho_{4f}$ (solid yellow circles) is obtained by subtracting $\rho$ of $LaTi_2Al_{20}$ from that of $PrTi_2Al_{20}$. The resistivity of $LaTi_2Al_{20}$ is measured down to 2 K. To obtain $\rho_{4f}$ below 2 K, we estimated the resistivity of $LaTi_2Al_{20}$ below 2 K based on the $T^2$ fit ($\rho = \rho_0 + AT^2$) shown in the inset, with fitting parameters $A = 1.7 \times 10^4$ μΩ cm/K$^2$ and $\rho_0 = 0.31$ μΩ cm. The downward arrow marks the ferroquadrupolar (FQ) transition temperature $T_Q \sim 2$ K. The solid black line represents the Fermi liquid behavior $\rho_{4f} \propto T^2$. The inset shows $\rho$ vs $T^2$ for $PrTi_2Al_{20}$ (yellow circles) and $LaTi_2Al_{20}$ (blue circles). The solid black lines represent the $T^2$ fits at 7 K $\leqslant T \leqslant$ 17 K for $PrTi_2Al_{20}$ and 2 K $\leqslant T \leqslant$ 20 K for $LaTi_2Al_{20}$.

## II. RESULTS AND DISCUSSION

### A. Resistivity and magnetoresistance experiments

Figure 1 shows the temperature $T$ dependence of the zero-field resistivity $\rho$ for $PrTi_2Al_{20}$ and $LaTi_2Al_{20}$. The zero-field Pr-$4f$ electron contribution to the resistivity, $\rho_{4f}(T)$, is obtained by subtracting the resistivity curve of the isostructural, non-$4f$ analog $LaTi_2Al_{20}$ from the raw data of $PrTi_2Al_{20}$. In the high-$T$ regime of $T \gtrsim \Delta_{CEF} \sim 60$ K, $\rho_{4f}(T)$ shows a logarithmic increase in cooling and reaches a broad peak at $T \sim \Delta_{CEF}$. The behavior of $\rho_{4f}(T)$ in this $T$ regime is governed by the magnetic Kondo effect arising from the excited magnetic triplets [18]. Below $\Delta_{CEF} \sim 60$ K, the excited triplet states become less relevant, leading to competing multipolar and magnetic Kondo effects. As a result, $\rho_{4f}(T)$ settles into a Fermi liquid (FL) regime with $\sim T^2$ behavior for 7 K $\lesssim T \lesssim$ 17 K, rather than exhibiting the $\sim T^{1/2}$ non-Fermi-liquid behavior expected for a quadrupolar Kondo lattice [31] (Fig. 1, inset). The $T^2$ coefficient $A$ is about 200 times the value found in $LaTi_2Al_{20}$, consistent with the heavy fermion formation reported in previous specific heat and dHvA experiments [23,27]. The sharp exponential decay of $\rho_{4f}(T)$ below $T_Q \sim 2$ K marks the entry into the FQ ordered state with ceased quadrupolar-fluctuation scattering. We note that $\rho(T)$

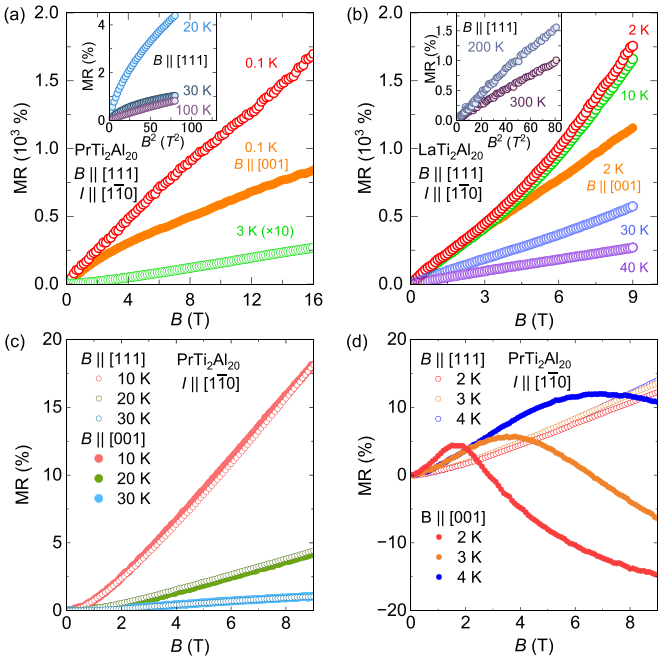


FIG. 2. (a) Transverse magnetoresistance (MR) curves of $PrTi_2Al_{20}$ obtained at representative temperatures. The main panel shows the MR measured at 0.1 and 3 K under $B \parallel [111]$ (open symbols) and at 0.1 K under $B \parallel [001]$ (orange solid symbols). The 3-K curve is magnified by a factor of 10 for clarity. The inset shows the MR curves obtained above the FQ transition for $B \parallel [111]$. (b) MR curves of $LaTi_2Al_{20}$ for temperature range from 2 to 40 K under $B \parallel [111]$ (open symbols) and 2 K under $B \parallel [001]$ (orange solid symbols). The inset shows the MR curves obtained for $T \gtrsim 200$ K for for $B \parallel [111]$. (c) and (d) Magnetic field $B$ dependence of the MR for $PrTi_2Al_{20}$ measured in $B \parallel [111]$ (open symbols) and $B \parallel [001]$ (solid symbols) at $T \geqslant 10$ K (c) and $T \leqslant 4$ K (d).

deviates from the $T^2$ dependence and shows upward convex curvature $\rho \sim T^n$ ($n \lesssim 1$) for $T_Q < T \lesssim 7$ K. This behavior can be attributed to a crossover from the FL state driven by competing magnetic and quadrupolar Kondo effects to a non-Fermi-liquid (NFL) state stemming from the quadrupolar Kondo effect, as predicted by numerical renormalization group calculations [32,33]. Previous specific heat measurements reveal an entropy release in the same temperature range, supporting this scenario [18]. In the close neighborhood of $T_Q$, critical quadrupolar fluctuations associated with the FQ transition might also influence the behavior of $\rho(T)$, while their effects are unlikely to persist up to as high as 7 K. The overall behavior of $\rho_{4f}(T)$ is consistent with the previous report [18].

The transverse MR of $PrTi_2Al_{20}$ measured under $B \parallel [111]$ and $B \parallel [001]$ is shown in Figs. 2(a), 2(c), and 2(d). We first focus on the behavior observed for $B \parallel [111]$. In the high-$T$ regime dominated by the magnetic Kondo effect, the MR exhibits quadratic field dependence MR $\propto B^2$ [Figs. 2(a), inset and 6(a)]. Once the multipolar Kondo effect kicks in below $\Delta_{CEF} \sim 60$ K, the MR develops a crossover from the low-field $B^2$ behavior to a quasilinear field dependence [Fig. 2(a)]; the crossover shifts to a lower field on cooling. Below $T_Q \sim 2$ K, the window of $B^2$ behavior completely vanishes, and unsaturated quasilinear MR persists up to 16 T. Remarkably, the magnitude of MR undergoes three-orders-of-magnitude enhancement across the FQ transition, reaching $\sim 10^3\%$ at 0.1 K [Fig. 2(a)]; this value falls in the typical range $10^3$–$10^8\%$ of extremely large magnetoresistance (XMR) [3]. The MR observed for $B \parallel [001]$ is nearly identical to that for $B \parallel [111]$ for $T \gtrsim 10$ K [Fig. 2(c)]. Below $T_Q$, XMR on the order of $\sim 10^3\%$ also emerges for $B \parallel [001]$, but with clear anisotropy compared with $B \parallel [111]$ [Fig. 2(a), main panel], which will be discussed in detail later.

Though XMR is extensively explored in topological and two-dimensional materials, it has not yet been reported in a pure orbital ordered phase. Thus, identifying the mechanism behind the observed XMR in $PrTi_2Al_{20}$ may help widen the scope of XMR studies. To explore the mechanism behind the observed XMR, we make a comparison with the magnetotransport behavior in the non-$4f$ analog $LaTi_2Al_{20}$. As shown in Figs. 2(b) and 6(b), for both $B \parallel [111]$ and $B \parallel [001]$, the MR of $LaTi_2Al_{20}$ follows $B^2$ behavior up to 9 T for $T \gtrsim 200$ K and develops a crossover from $B^2$ to nearly $B$-linear dependence on cooling; unsaturated XMR on the order of $10^3\%$ takes place in the FL state below 20 K (see Fig. 1, inset, for the FL fit). Owing to the lack of $4f$ multipolar moments in $LaTi_2Al_{20}$, this close resemblance suggests that the XMR arises from some common characteristics of the two materials that are insensitive to the presence of multipolar moments and their long-range FQ order at the low-$T$ limit. Moreover, the $c$-$f$ hybridization tends to decline sharply in the FQ ordered state, evident from the previous specific heat measurements showing that the residual entropy associated with the quadrupolar Kondo effect is released in the FQ ordered state, as well as the gapped behavior (i.e., exponential decay) of $\rho(T)$ (Fig. 1) and specific heat below the FQ transition temperature $T_Q$ [18]. Thus it appears unlikely that the interaction between multipolar moments and conduction electrons plays a major role in producing the XMR in the FQ ordered state of $PrTi_2Al_{20}$.

Electron-hole compensation and ultrahigh carrier mobility [in the range $10^4$–$10^6$ cm$^2$/(V s)] are the two most common mechanisms that generate XMR [3]. These are often realized in semimetals featuring small Fermi pockets and low density of states (DOS) near the Fermi level [7,10,34–37]. However, both $PrTi_2Al_{20}$ and $LaTi_2Al_{20}$ are metallic systems with sizable FS sheets and DOS near the Fermi level [27], unlikely to reach the ultrahigh mobility as in the semimetal cases. Moreover, carrier compensation or high mobility alone typically yields unsaturated, quadratic MR $\sim B^2$, inconsistent with the observed quasilinear field dependence shown in Fig. 2. Exceptions may occur for topological Dirac and Weyl semimetals, in which the linear band dispersion can lead to unsaturated linear-in-$B$ MR [7,34], while this situation does not apply to the band structures of $PrTi_2Al_{20}$ or $LaTi_2Al_{20}$. Thus carrier compensation or high mobility is insufficient to explain the nonsaturating linear XMR observed here; another factor is at play for its generation.

Given that $PrTi_2Al_{20}$ has no spin degrees of freedom in its CEF ground state and shows no trace of charge order at low $T$'s [21,22,38], we can also rule out spin fluctuations and charge density waves as possible mechanisms for the observed XMR. We then turn to the FS properties given that

the previous dHvA study suggests similar FS geometry for $PrTi_2Al_{20}$ and $LaTi_2Al_{20}$. In particular, we consider the possibility of enhanced MR due to open-orbit FS topology [39–41]. The previously reported FS of $LaTi_2Al_{20}$ comprises a large jungle-gym-like electron sheet (96th band), with cubic symmetry and "necks" along the eight symmetrically equivalent ⟨111⟩ axes [27], bearing similarity with the well-studied FS of copper [42,43]. Such necks in the FS can induce open orbits for the FS cross section in a certain range of magnetic field, leading to complex field angle dependence of the XMR. In the copper case, when $B \parallel \langle 001 \rangle$, the MR value is at a minimum with a convex upward curvature. As $B$ rotates from ⟨001⟩ to ⟨110⟩, the MR can exhibit unsaturated, quasilinear field dependence for some intermediate angles (such as $B \parallel \langle 111 \rangle$) before reaching a maximum with quadratic field dependence [42,43]. Thus the open-orbit FS topology well accounts for the quasilinear XMR and its anisotropy between $B \parallel [111]$ and $B \parallel [001]$ at the low-$T$ limit. The similar MR behavior observed in $PrTi_2Al_{20}$ and $LaTi_2Al_{20}$ at the low-$T$ limit suggests that such open-orbit FS topology persists even with $c$-$f$ hybridization and the long-range FQ order, serving as a key driver of the nonsaturating, linear XMR in $PrTi_2Al_{20}$.

We note that quantum oscillations emerge in MR and the Hall effect below ∼1 K in $PrTi_2Al_{20}$ (see details in the Appendix and Fig. 12). The observable quantum oscillations indicate that the system fulfills the high-field limit in the FQ ordered state, namely, $\omega_c \tau \gtrsim 2\pi$, where $\omega_c$ is the cyclotron frequency and $\tau$ is the scattering time. Under this condition, the carriers can traverse a complete cyclotron orbit before being scattered, allowing the open-orbit FS geometry to be reflected in the magnetotransport, consistent with the presence of open-orbit-induced linear XMR within the FQ state. Moreover, the crossover in MR from $B^2$ to $B$-linear behavior on cooling leads to a violation of the ordinary and extended Kohler's rules (Appendix and Fig. 7). Violation of the Kohler's rule is typically associated with changes in the anisotropy pattern of the scattering time $\tau(\mathbf{k})$ on the FS, as reported in cuprates and iron-based superconductors [44,45]. This scenario is again in line with more carriers moving along the open-orbit trajectories on the FS as inelastic and orbital-fluctuation-induced scatterings cease in the low-$T$ FQ state.

Interestingly, the MR of $PrTi_2Al_{20}$ is nearly isotropic at high $T$'s but becomes strongly anisotropic on approaching the FQ order [Figs. 2(c) and 2(d)]: For $T_Q \lesssim T < 10$ K, the MR increases monotonically under $B \parallel [111]$, whereas it forms a broad maximum and then declines at higher fields under $B \parallel [001]$. Within the FQ order, the MR curve displays a kink around $B = 2$ T $\parallel [001]$ [Fig. 2(a)], whereas this anomaly is absent for $B \parallel [111]$; the difference in magnitude reaches nearly twofold at 16 T for the two field directions. The low-field MR anomaly overlaps with a field-induced transition previously detected by NMR and magnetization around $B = 2$ T $\parallel [001]$, whereas such a transition is absent for $B \parallel [111]$ [22,30]. We note that the MR exhibits weak residual resistivity ratio (RRR) dependence for high-quality single crystals (Fig. 9), and thus the observed anisotropy is intrinsic rather than caused by the difference in sample quality. The low-temperature MR anisotropy observed in $PrTi_2Al_{20}$ [Figs. 2(a) and 2(d)] is more pronounced than the anisotropy observed in $LaTi_2Al_{20}$ [Figs. 2(b) and 6(b)], suggesting that

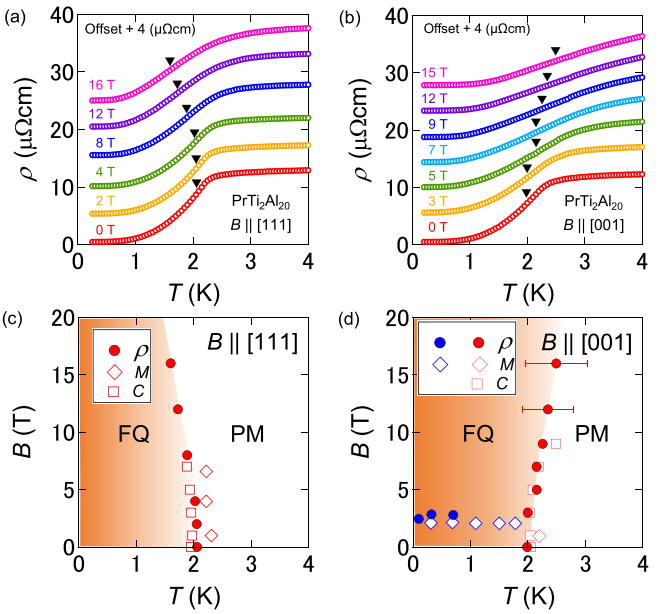


FIG. 3. (a) and (b) Temperature $T$ dependence of the resistivity $\rho(T)$ in $PrTi_2Al_{20}$ measured below 4 K under $B \parallel [111]$ (a) and $B \parallel [001]$ (b). The curves are vertically shifted by 4 μΩ cm/K for each finite field value. Downward black triangles mark the FQ transition determined from the peaks of the resistivity derivative $d\rho/dT$ (see Fig. 8). (c) and (d) The temperature-field ($T$-$B$) phase diagram of $PrTi_2Al_{20}$ obtained in $B \parallel [111]$ (c) and $B \parallel [001]$ (d). The red solid circles represent the FQ-PM phase boundary derived from the temperature dependence of $\rho$ [i.e., the black triangles in (a) and (b)]. The blue solid circles represent the field-induced transition around 2 T obtained from the MR measurements; the open symbols are based on previously reported magnetization ($M$; open diamonds) and specific heat measurements ($C$; open squares) [18,22].

the $4f$ multipolar moments, along with their remaining interaction with the conduction electron sea in the ordered state, could offer an additional mechanism for the magnetotransport anisotropy in $PrTi_2Al_{20}$ other than the open-orbit FS topology.

### B. Temperature-field phase diagrams

To further investigate the anisotropic low-$T$ transport in $PrTi_2Al_{20}$, we outline the highly anisotropic temperature-field ($T$-$B$) phase diagrams under $B \parallel [111]$ and $B \parallel [001]$ based on isofield resistivity measurements [Figs. 3(a), 3(b), and 8]. The phase diagrams based on transport data shown in Figs. 3(c) and 3(d) agree with those obtained by previous NMR and thermodynamic measurements [18,22,30]. For $B \parallel [111]$, the FQ transition remains well defined up to ∼10 T, with $T_Q$ decreasing as $B$ rises beyond 5 T [Figs. 3(a), 3(c), 8(a), 8(c)]. In contrast, the long-range FQ order is "soft" for $B \parallel [001]$. A small field of $B \sim 2$ T $\parallel [001]$ turns the second-order FQ transition into a smooth crossover, evidenced by the drastic broadening of the resistivity anomaly at $T_Q$ [Figs. 3(b), 8(b), and 8(d)]; the FQ-paramagnet (PM) phase boundary bends toward higher $T$ with increasing $B$ [Fig. 3(d)]. The observed anisotropic field evolution of the FQ-PM transition boundary results from the strongly anisotropic response of the FQ order to [111] and [001] magnetic fields,

which can be explained by the competition between the Zeeman effect and the field-induced quadrupolar-quadrupolar interaction [22]. The possibility for a metastable domain structure is also discussed theoretically [46]. The quadrupolar short-range fluctuations associated with the crossover under $B \parallel [001]$ can alter the carrier scattering and thereby the magnetotransport near $T_Q \sim 2$ K, leading to the sharply different behavior of MR compared with that in $B \parallel [111]$.

Below $T_Q \sim 2$ K, the MR anomaly near 2 T for $B \parallel [001]$ [Fig. 2(a)] is likely associated with a change in the quadrupolar ordering structure [22,30,47]. Earlier comparison of the NMR and specific heat results with theoretical analysis suggests that the low-field transition might be driven by FQ order parameter switching accompanied by a change in the $c$-$f$ hybridization, which may cause FS reconstruction [22,30]. Then the difference in quadrupolar ordering structure between the [111] and [001] directions can induce the transport anisotropy via modifying the anisotropy pattern of the scattering rate on the FS.

### C. Hall effect experiments

The Hall resistivity may offer more insight into the interplay of multipolar order with FS and transport properties. $PrTi_2Al_{20}$ is ideal for investigating the Hall effect in a multipolar heavy fermion system, which has yet to be explored. Figure 4(a) shows the magnetic field $B$ dependence of the Hall resistivity $\rho_H$ for $PrTi_2Al_{20}$ at various temperatures, and the $B$ dependence of the Hall coefficient $R_H \equiv \rho_H/B$ of $PrTi_2Al_{20}$ obtained at selected temperatures is shown in Fig. 4(c). $R_H$ shows clear $B$ dependence, reflecting nonlinear $\rho_H$ as a function of $B$. Such nonlinearity indicates the multiple-band signature, as discussed below. The high-field anomaly at ∼11 T [Figs. 4(a) and 4(c)] is likely related to a field-induced rearrangement of multipolar moments within the FQ ordered phase, similar to the transition reported for the sister compound $PrV_2Al_{20}$ under $B \sim 11$ T $\parallel [001]$ [29,48]. Further experiments on detecting the FQ order parameter are necessary to confirm this scenario.

Next, we explore the temperature dependence of the initial Hall coefficient $R_H^0$ for $PrTi_2Al_{20}$ [Fig. 4(e)], where $R_H^0$ is defined as the slope of the Hall resistivity versus field isothermals at the zero-field limit. $R_H^0$ is positive in the entire measured $T$ range, indicating hole-type majority charge carriers. With decreasing $T$, $R_H^0$ exhibits a mild increase below $\Delta_{CEF} \sim 60$ K, then forming a plateau in the FL state ($7\ \text{K} \lesssim T \lesssim 17$ K); a more pronounced upturn of $R_H^0$ occurs near $T_Q \sim 2$ K, followed by saturation in the ordered state.

Such a temperature dependence of $R_H^0$ is qualitatively distinct from the behavior typically seen in magnetic heavy fermion metals [49]. The Hall coefficient consists of the normal Hall component $R_H^N$ and the anomalous Hall component $R_H^A$. As shown by the dashed lines in Fig. 4(e), the initial Hall coefficient $R_H^0$ of various classes of magnetic heavy fermion compounds displays a common feature [49]: a broad maximum near the coherence temperature $T_{coh}$, marking a crossover from the high-$T$ regime dominated by the skew-scattering-induced anomalous Hall effect $R_H^A$ to the low-$T$ coherence regime where $4f$ moments enter the Fermi volume, forming a heavy FL. In the high-$T$ regime, the $R_H^A$ is well

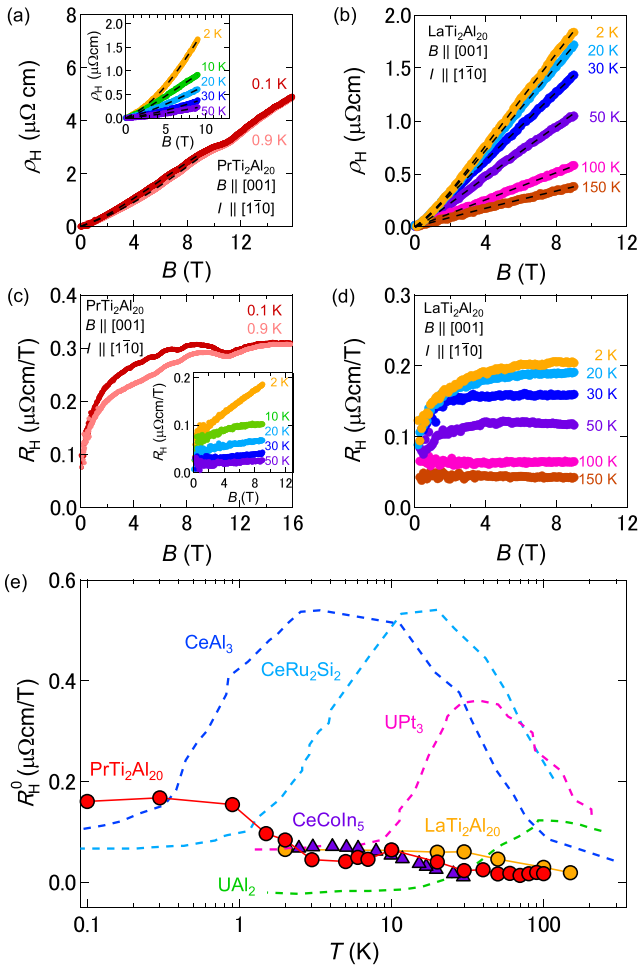


FIG. 4. (a) Magnetic field $B$ dependence of the Hall resistivity $\rho_H$ and (b) the Hall coefficient $R_H$ of $PrTi_2Al_{20}$ obtained at representative temperatures in $B \parallel [001]$. The main panel shows $\rho_H$ obtained within the FQ ordered phase at 0.1 and 0.9 K, and the inset shows $\rho_H$ measured above the FQ transition. The black dashed lines represent the two-band fits performed for 0–9 T, avoiding the high-field anomaly centered at ∼11 T. (c) Magnetic field $B$ dependence of $\rho_H$ and (d) $R_H$ of $LaTi_2Al_{20}$ measured under $B \parallel [001]$ in the temperature range from 2 to 150 K. (e) The initial Hall coefficient $R_H^0$ of $PrTi_2Al_{20}$ (red solid symbols) and $LaTi_2Al_{20}$ (orange solid symbols) obtained from the slope of the isothermal $\rho_H$ vs $B$ curves in the zero-field limit. Dashed lines are $R_H^0$ for representative Ce- and U-based heavy fermion compounds [49].

scaled by the magnetic susceptibility, such that $R_H^A \propto \chi$ or $R_H^A \propto \chi\rho$, where $\rho$ is the longitudinal resistivity. In contrast, the coherence peak is absent in $R_H^0$ of $PrTi_2Al_{20}$, and $R_H^0$ cannot be scaled by either $\chi$ or $\chi\rho$ [Figs. 5(a), 5(b), and 10] [49]. Thus the anomalous Hall component associated with the magnetization is negligibly small at least below 100 K in $PrTi_2Al_{20}$, as expected from the lack of dipolar degrees of freedom in its CEF ground-state doublet and the sizable gap $\Delta_{CEF} \sim 60$ K between the ground-state doublet and the first-excited magnetic triplet. Moreover, the overall field dependence and magnitude of $\rho_H$ and the Hall coefficient $R_H \equiv \rho_H/B$ in the FQ ordered state of $PrTi_2Al_{20}$ are similar to that of $LaTi_2Al_{20}$ [Fig. 5(a)], indicating that the anomalous

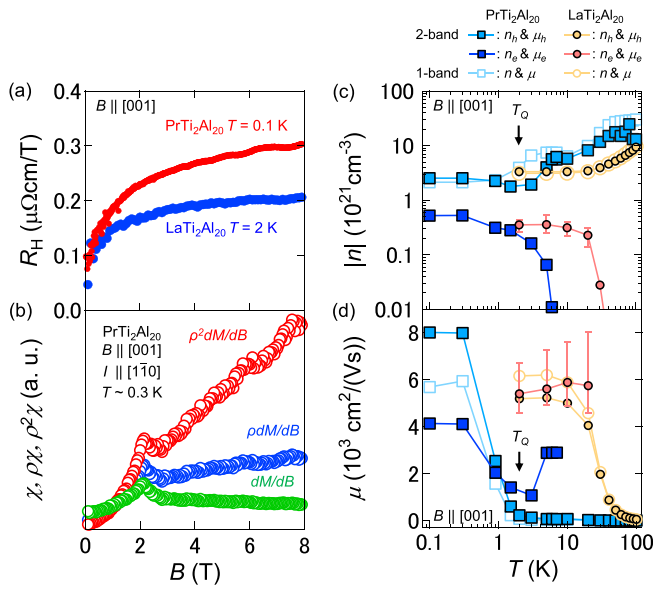


FIG. 5. (a) Low-$T$ Hall coefficient $R_H$ vs $B$ of $PrTi_2Al_{20}$ and $LaTi_2Al_{20}$ compared with (b) the $B$ scaling of the magnetic susceptibility $\chi$ and the quantities $\chi\rho$ and $\chi\rho^2$ of $PrTi_2Al_{20}$ measured at 0.3 K. (c) The evolution of the charge carrier density $|n|$ and (d) mobility $\mu$ as a function of temperature $T$ estimated based on the two-band fits with fitting range $0\ \mathrm{T} \leqslant B \leqslant 9\ \mathrm{T}$ (solid symbols) in $LaTi_2Al_{20}$ (orange, $n_e$ and $\mu_e$; yellow, $n_h$ and $\mu_h$) and $PrTi_2Al_{20}$ (dark blue, $n_e$ and $\mu_e$; light blue, $n_h$ and $\mu_h$) and from the initial Hall coefficient $R_H^0$ (i.e., one-band fitting) in $LaTi_2Al_{20}$ (open yellow circles) and $PrTi_2Al_{20}$ (open light blue squares). The one-band fitting yields dominated hole-type charge carriers, consistent with the two-band fitting results.

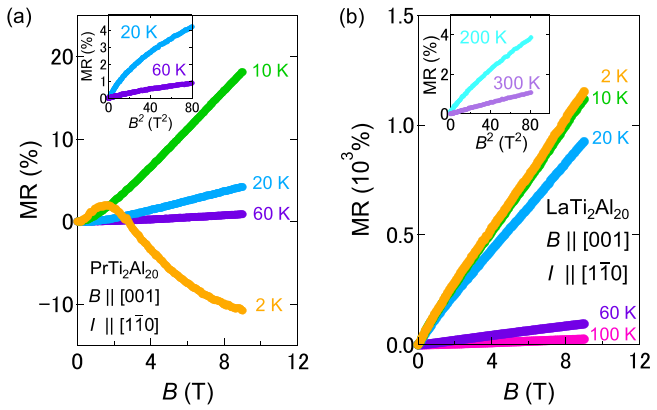


FIG. 6. Transverse magnetoresistance (MR) measured under $B \parallel [001]$ in $PrTi_2Al_{20}$ (a) and $LaTi_2Al_{20}$ (b). Insets show $B^2$ dependence of transverse MR measured under $B \parallel [001]$ for $PrTi_2Al_{20}$ at $T =$ 20 K and 60 K (a) and $LaTi_2Al_{20}$ at $T \geqslant 200$ K (b).

Hall contribution from the high-rank multipolar moments has minor influence on the low-$T$ Hall effect. Altogether, our findings indicate that $R_H$ of $PrTi_2Al_{20}$ is governed by the normal Hall contribution $R_H^N$, which is the same as in $LaTi_2Al_{20}$, which allows comparison of the Hall coefficient behavior in the two systems.

The normal Hall effect yields information about carrier density and mobility. In the high-field limit $\omega_c\tau \gtrsim 2\pi$, the Hall coefficient $R_H$ reaches a field-independent value, $R_H(\infty) = \frac{1}{e(n_h - n_e)}$, that provides a measure of the net carrier density enclosed by the FS. For both $B \parallel [001]$ and $B \parallel [111]$, the $\rho_H$ of $PrTi_2Al_{20}$ becomes nonlinear in $B$ for $T_Q < T <$ 50 K, and its magnitude is strongly $T$ dependent [Figs. 4(a), inset and 11(a), inset]. Such nonlinearity is more pronounced than that observed in $LaTi_2Al_{20}$ [Figs. 4(b) and 11(c)], suggesting carrier mobility misbalances on the electron and hole FS sheets due to the interplay between $4f$ quadrupolar moments and conduction electrons. Moreover, $R_H$ of $PrTi_2Al_{20}$ does not fully saturate up to 9 T [Figs. 4(c), inset and 11(b), inset], in contrast with $R_H$ in $LaTi_2Al_{20}$, which levels off at $\sim$3 T [Figs. 4(d) and 11(d)]; namely, a higher $B$ is necessary for $PrTi_2Al_{20}$ to reach the high-field limit. These facts suggest that the transport properties above $T_Q$ are strongly affected by substantial quadrupolar fluctuations as an additional scattering mechanism. This point is corroborated by the abovementioned MR crossover in $PrTi_2Al_{20}$ from low-field $B^2$ dependence to quasi-$B$-linear dependence without saturation in the same $T$ range [Figs. 2(a), inset and 6(a)].

With suppressed quadrupolar fluctuations below $T_Q$, the isothermal field sweeps of $\rho_H(B)$ become nearly $T$ independent but still exhibit nonlinearity [Fig. 4(a), main panel]. For $B \parallel [001]$, the Hall coefficient $R_H$ [Figs. 4(c), main panel, and 5(a)] displays a smooth crossover from the low-field increase to a field-independent regime above $\sim$8 T; the high-field $R_H$ value is larger than that of $LaTi_2Al_{20}$, indicating a lower net carrier density in the FQ ordered state. This feature indicates that the $4f$ moments only weakly contribute to the Fermi volume below $T_Q$. Unlike the magnetic susceptibility shown in Fig. 5(b), $R_H$ does not exhibit any sharp anomaly at $B \sim 2$ T $\parallel [001]$; therefore the field-induced change in quadrupolar ordering structure does not seem to trigger noticeable FS reconstruction, possibly owing to the strongly suppressed $c$-$f$ hybridization below $T_Q$ [18].

The multiband effect is a typical mechanism for the nonlinear $B$ dependence of the normal Hall effect. We therefore estimate the carrier densities and mobilities by fitting $\rho_H$ to the widely used two-band model that simplifies the multiband scenario into one electron-type band and one hole-type band [42,50], such that

$$\rho_H(B) = \frac{B}{e}\frac{\left(n_h\mu_h^2 - n_e\mu_e^2\right) + (n_h - n_e)\mu_e^2\mu_h^2B^2}{(n_h\mu_h + n_e\mu_e)^2 + (n_h - n_e)^2\mu_e^2\mu_h^2B^2}, \qquad (1)$$

where $n_{e,h}$ are the electron-type and hole-type carrier densities and $\mu_{e,h}$ are their respective mobilities (see details in the Appendix). Though the two-band fitting cannot fully capture the complex multiband FS of $PrTi_2Al_{20}$ and $LaTi_2Al_{20}$, it reasonably estimates the carrier properties (see Table I) [27]. We note that the field range of the fits is limited to $0\ \mathrm{T} \leqslant B \leqslant 9\ \mathrm{T}$ to avoid inclusion of the high-field anomaly located around $\sim$11 T. The electron and hole densities and mobilities obtained from the two-band fit are shown in Figs. 5(c) and 5(d), compared with the results estimated from the initial Hall coefficient $R_H^0$ (i.e., the one-band model). The increasing deviation between the two-band and one-band fitting results reflects the

TABLE I. Low-$T$ limit electron and hole carrier densities obtained from experiments and first-principle calculation in $PrTi_2Al_{20}$ and $LaTi_2Al_{20}$.

| | $PrTi_2Al_{20}$ (Experiment) | $LaTi_2Al_{20}$ (Experiment) | $LaTi_2Al_{20}$ (Calculation [27]) |
|---|---|---|---|
| $n_e$ ($10^{20}$ 1/cm$^3$) | ∼5.2 | ∼3.6 | ∼6.7 |
| $n_h$ ($10^{20}$ 1/cm$^3$) | ∼25 | ∼33 | ∼7.2 |

nonlinear field dependence of $\rho_H$ at low $T$'s, originating from the multiband effect.

For both $PrTi_2Al_{20}$ and $LaTi_2Al_{20}$, the hole band dominates the electrical transport process at all measured $T$'s. The electronlike contribution $n_e$ becomes appreciable near $T_Q$ in $PrTi_2Al_{20}$ [Fig. 5(c)]; the electron and hole mobilities, $\mu_e$ and $\mu_h$, are both dramatically enhanced on cooling below $T_Q$, then leveling off in the FQ ordered state [Fig. 5(d)]. These results support the scenario that the suppression of quadrupolar-fluctuation-induced scatterings below $T_Q$ leads to sufficiently high carrier mobilities, which are necessary for observing the linear XMR induced by open-orbit trajectories on the large electronlike FS sheet. The qualitative behavior and low-$T$ values of carrier densities and mobilities in $LaTi_2Al_{20}$ resemble the behavior in $PrTi_2Al_{20}$. A key difference is that the enhancement of the electron-band contribution appears at much higher temperatures ($T \lesssim 70$ K) in $LaTi_2Al_{20}$ [Figs. 5(c) and 5(d)], likely due to the lack of quadrupolar fluctuations. This difference naturally explains why the onset of XMR occurs at a lower temperature in $PrTi_2Al_{20}$ than in $LaTi_2Al_{20}$. Moreover, the electron and hole mobilities overlap in $LaTi_2Al_{20}$ but differ ($\mu_e < \mu_h$) in the low-$T$ regime in $PrTi_2Al_{20}$, which explains the stronger nonlinearity of $\rho_H(B)$ in $PrTi_2Al_{20}$. The imbalanced $\mu_e$ and $\mu_h$ in $PrTi_2Al_{20}$ might result from the mildly enhanced $m^*$ on the electron FS, the anisotropic scattering time $\tau$ induced by the quadrupolar order parameter, or both.

Similar to the MR, the Hall resistivity $\rho_H(B)$ in the FQ ordered phase of $PrTi_2Al_{20}$ is strongly anisotropic in [001] and [111] magnetic fields: For $B \parallel [111]$, the $\rho_H(B)$ shows concave curvature above ∼4 T, and its magnitude at 0.1 K is only about one-third of that for $B \parallel [001]$ [Figs. 11(a) and 11(b)]. The simple two-band scenario cannot describe the field dependence of $\rho_H(B)$ under $B \parallel [111]$. Again, such a pronounced anisotropy is absent in $LaTi_2Al_{20}$ [Figs. 4(b), 4(d), 11(c), and 11(d)], implying that the anisotropic transport in $PrTi_2Al_{20}$ originates from the field-induced change of FQ order structure under $B \parallel [001]$.

## III. CONCLUSION

To summarize, our comprehensive study of magnetotransport in $PrTi_2Al_{20}$ reveals extremely large magnetoresistance (XMR) reaching $\sim 10^3$% in its FQ ordered state. Based on comparison with the non-4$f$ analog, $LaTi_2Al_{20}$, we attribute this XMR to the open-orbit topology of the Fermi surface. The $B$ dependence of the Hall resistivity $\rho_H$ displays stronger nonlinearity than that of $LaTi_2Al_{20}$ on approaching the FQ state. Analysis using the two-band model indicates that the contribution from the electron-type FS sheet featuring open orbits becomes effective upon suppression of the quadrupolar-fluctuation scattering, further supporting the FS topology's key role in generating the XMR. Both the MR and $\rho_H$ become highly anisotropic under $B \parallel [111]$ and $B \parallel [001]$ in the FQ state, following the distinct response of the FQ order parameter under the two field orientations. Our study indicates that the multipolar ordered state without involving spin degrees of freedom can realize large magnetoresistance. These findings provide essential insights that may help in identifying universal mechanisms behind large magnetotransport phenomena and thereby widen their applications.

## ACKNOWLEDGMENTS

This work is partially supported by CREST (Grant No. JPMJCR18T3), Japan Science and Technology Agency; by Grants-in-Aid for Scientific Research on Innovative Areas (Grants No. 15H05882 and No. 15H05883) from the Ministry of Education, Culture, Sports, Science and Technology of Japan; and by Grants-in-Aid for Scientific Research (Grant No. 19H00650) from the Japanese Society for the Promotion of Science (JSPS). This work is partially supported by JSPS KAKENHI Grant No. 20K03829. T.I. is supported by JST SPRING, Grant No. JPMJSP2108. M.F. acknowledges support from the Japan Society for the Promotion of Science Postdoctoral Fellowship for Research in Japan (Standard).

## APPENDIX A: MATERIALS AND METHODS

We grew $PrTi_2Al_{20}$ and $LaTi_2Al_{20}$ single crystals by the Al self-flux technique, as previously reported [18]. Four pieces of high-quality samples are selected for the transport measurements; the $PrTi_2Al_{20}$ samples have zero-field residual resistivity ratios (RRR) of ∼130 and ∼120, with the [111] and [001] orientations, respectively; the two $LaTi_2Al_{20}$ samples also have similar RRR of ∼130–140. The magnetoresistivity and Hall effect were measured under applied magnetic fields up to 16 T along the [111] or [001] direction with a standard six-point contact geometry. The applied electrical current is perpendicular to the field direction. DC resistivity measurements from 2 K up to room temperature were performed using a physical property measurement system (PPMS, Quantum Design). The low-temperature range below 2 K down to 0.1 K was covered using a $^3$He–$^4$He dilution refrigerator (Kelvinox 25, Oxford instruments), and AC resistivity measurements are preformed using a lock-in amplifier (SR830, Stanford research systems). We have confirmed consistency for the resistivity data obtained using the two measurement methods. The studied samples do not show a superconducting transition down to 0.1 K, possibly due to residual magnetic field in the superconducting magnet that is typically comparable to the small upper critical field (∼6 mT) in $PrTi_2Al_{20}$ [23]. The transverse MR is defined as $\mathrm{MR}(\%) \equiv \Delta\rho_{xx}(B)/\rho_{xx}(0) \times 100$. The Hall contribution to the resistance is extracted

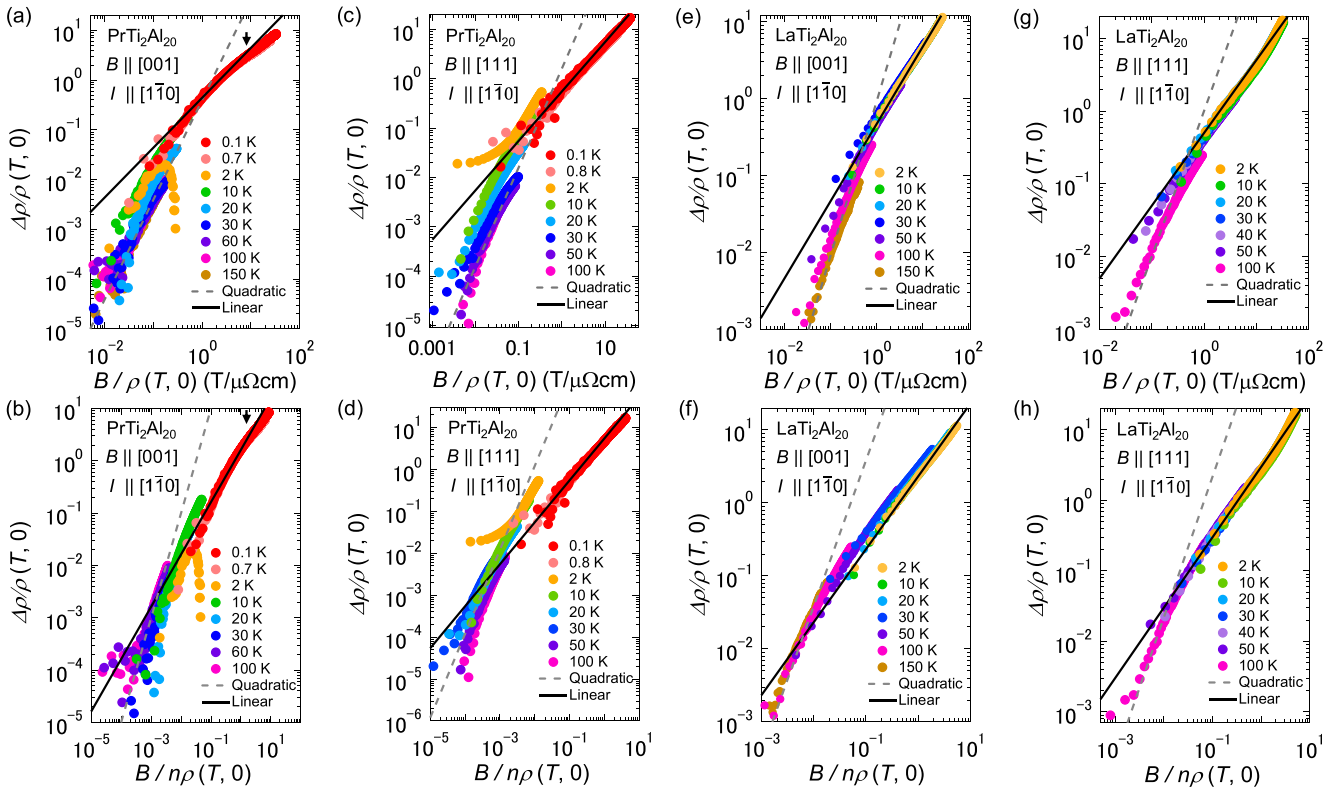


FIG. 7. (a)–(d): Ordinary Kohler's plot for $PrTi_2Al_{20}$ at $B \parallel [001]$ (a) and $B \parallel [111]$ (b), and for $LaTi_2Al_{20}$ at $B \parallel [001]$ (c) and $B \parallel [111]$ (d). (e)–(h): Extended Kohler's plot for $PrTi_2Al_{20}$ at $B \parallel [001]$ (e) and $B \parallel [111]$ (f), and for $LaTi_2Al_{20}$ at $B \parallel [001]$ (g) and $B \parallel [111]$ (h). The black solid and grey dashed lines represent linear and quadratic scaling of MR, respectively. Black arrows indicate an additional deviation from linear scaling in (a) and (e).

by subtracting the resistance of positive and negative field scans.

## APPENDIX B: ORDINARY AND EXTENDED KOHLER'S SCALING ANALYSIS FOR $B \parallel [001]$ and $B \parallel [111]$

Figure 6 shows the transverse magnetoresistance (MR) of $PrTi_2Al_{20}$ [Fig. 6(a)] and $LaTi_2Al_{20}$ [Fig. 6(b)] measured at selected temperatures under $B \parallel [001]$. Together with the data measured in $B \parallel [111]$ (Fig. 2 in the main text), these MR data are used to generate Kohler's scaling analysis shown in Fig. 7.

Figures 7(a)–7(d) show the ordinary Kohler's plots for $PrTi_2Al_{20}$ and $LaTi_2Al_{20}$ measured in $B \parallel [001]$ and $B \parallel [111]$. On cooling, the MR curves of $PrTi_2Al_{20}$ [Fig. 7(a) and 7(b)] gradually deviate from $(B/\rho_{xx}(T,0))^2$ scaling for $T \lesssim 30$ K (grey dashed line) and collapse onto a curve that represents linear dependence on $(B/\rho_{xx}(T,0))$ (black solid line) in the FQ ordered state below $\sim$2 K. Similar behavior occurs in $LaTi_2Al_{20}$ [Fig. 7(c) and 7(d)].

We further perform the extended Kohler's analysis, MR vs $B/(n\rho)$, as shown in Figs. 7(e)–7(h), which considers the $T$ dependence of the carrier density $n$. The carrier density $n$ here is obtained from the initial Hall coefficient $R_H^0$; adopting the total carrier density $n = n_h + n_e$ obtained from the two-band fitting does not affect the analysis results. Similar to the ordinary Kohler's analysis, the extended Kohler's analysis does not yield a universal power-law relation and retains the crossover from the high-$T$ quadratic scaling to the low-$T$ linear scaling. The violation of Kohler's rule is consistent with the open-orbit scenario, as discussed in the main text. We note that the field-induced transition around 2 T $\parallel$ [001] in $PrTi_2Al_{20}$ causes an additional deviation from the linear scalings of $B/\rho(T,0)$ and $B/n\rho(T,0)$ at $T = 0.1$ K.

Figures 7(a)–7(d) show the ordinary Kohler's plot for $PrTi_2Al_{20}$ at $B \parallel [001]$ (a) and $B \parallel [111]$ (b), and for $LaTi_2Al_{20}$ at $B \parallel [001]$ (c) and $B \parallel [111]$ (d). (e)–(h) show the extended Kohler's plot for $PrTi_2Al_{20}$ at $B \parallel [001]$ (e) and $B \parallel [111]$ (f), and for $LaTi_2Al_{20}$ at $B \parallel [001]$ (g) and $B \parallel [111]$ (h). The black solid and grey dashed lines represent linear and quadratic scaling of MR, respectively. Black arrows indicate an additional deviation from linear scaling in (a) and (e).

## APPENDIX C: TEMPERATURE $T$ DEPENDENCE OF THE DERIVATIVE IN $PrTi_2Al_{20}$

Figures 8(a) and 8(b) show the temperature $T$ dependence of the the resistivity $\rho$ below 4 K measured under $B \parallel [111]$ (a) and $B \parallel [001]$ (b) to clarify origin of the negative MR for $B \parallel [001]$ around $T_Q \sim 2$ K. Figures 8(c) and 8(d) show the $T$ dependence of the the derivative $d\rho/dT$ below 4 K measured under $B \parallel [111]$ (c) and $B \parallel [001]$ (d). The anomaly due to the FQ order around 2 K corresponds to the peak in $d\rho/dT$. The anomaly for $B \parallel [001]$ broadens dramatically with increasing field, being suppressed by a much smaller field than that under $B \parallel [111]$. Such anisotropic behavior is

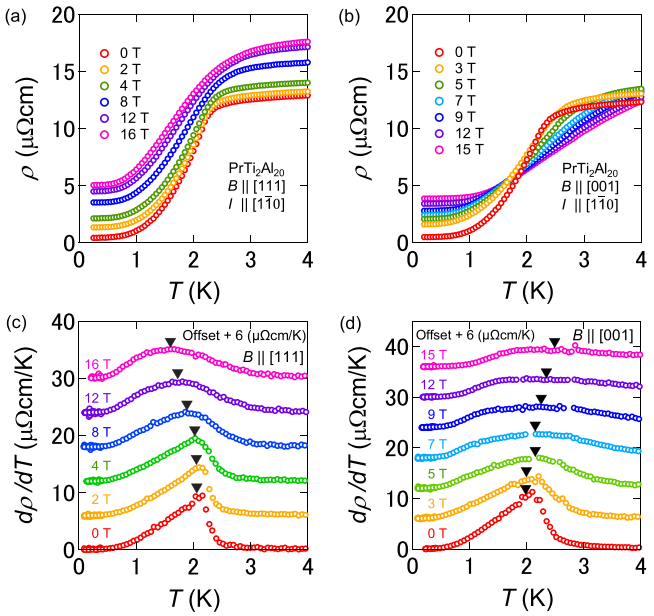


FIG. 8. (a) and (b): Temperature $T$ dependence of the resistivity $\rho$ in $PrTi_2Al_{20}$ measured at $T \leqslant 4$ K under $B \parallel [111]$ (a) and $B \parallel [001]$ (b). (c) and (d): Temperature $T$ dependence of the derivative $d\rho/dT$ in $PrTi_2Al_{20}$ measured at $T \leqslant 4$ K under $B \parallel [111]$ (c) and $B \parallel [001]$ (d), with a vertical shift of 6 $\mu\Omega$cm/K for each field value. Downward triangles indicate peaks of $d\rho/dT$, which determine the phase boundary of the FQ-PM transition in the $B$ - $T$ phase diagrams shown in the Figs. 3(c) and 3(d) of the main text.

in line with that observed in the low-$T$ MR [Fig. 2(d) in the main text].

## APPENDIX D: SAMPLE QUALITY DEPENDENCE OF MR FOR $PrTi_2Al_{20}$

Figure 9(a) shows the temperature dependence of normalized resistivity below 4 K for various $PrTi_2Al_{20}$ single crystals with different RRR. The exponential decay (i.e., gapped behavior) of the resistivity below the FQ transition strongly depends on the sample quality. Figures 9(b) and 9(c) shows the RRR dependence of MR for $PrTi_2Al_{20}$ at $T = 0.3$ K under $B \parallel [001]$ (b) and $B \parallel [111]$ (c). For both field directions, the overall $B$ dependence of the lower RRR samples is consistent with that of the higher RRR samples. The MR magnitude at 7 T$\parallel$ [001] is ∼440% for RRR ∼120 and about ∼380% for RRR ∼100; the difference is only about one-tenth of the magnitude. Therefore, the MR is weakly sample-dependent for high RRR values above 100. Given that the MR data shown in the main text are all taken on high-quality samples with RRR above 100, the observed anisotropic behavior between the two field directions (Fig. 2 in the main text) is an intrinsic property, not due to the sample quality dependence. In contrast, the MR value of the sample with a much lower RRR of ∼6 [Fig. 9(c), right axis] is about one order of magnitude smaller than that of the high-RRR sample. Thus, the realization of extremely large MR (XMR) in $PrTi_2Al_{20}$ requires sufficiently high sample quality, which is as expected because the magnitude of MR in metals typically depends on carrier mobility that relates directly to the sample quality.

## APPENDIX E: NEGLIGIBLE ANOMALOUS HALL CONTRIBUTION IN $PrTi_2Al_{20}$

It is known that the anomalous Hall coefficient $R_H^A$ shows a scaling relation with the magnetic susceptibility $\chi$, such as $R_H \propto \chi$, $R_H \propto \chi\rho$, or $\rho_{4f}^2 M/B$, where $\rho$ is the longitudinal resistivity. In Fig. 10, we examine such scaling relations of $R_H$ and found that the scaling relations do not hold in the measured $T$ range, indicating negligible anomalous Hall contribution in $PrTi_2Al_{20}$.

## APPENDIX F: HALL EFFECT FOR $B \parallel [111]$

Figures 11(a) and 11(b) show the magnetic field $B$ dependence of the Hall resistivity $\rho_H$ and Hall coefficient $R_H$ of $PrTi_2Al_{20}$ measured under $B \parallel [111]$. The $\rho_H(B)$ is slightly convexed above 2 K [Fig. 11(a), inset], while showing concave curvature above 4 T in the quadrupolar ordered state below 2 K, which contrasts strongly with the behavior observed for $B \parallel [001]$ [Figs. 4(a) and 4(c) in the main text]. Moreover, the magnitude of $\rho_H$ is only about one-third of that for $B \parallel [001]$. In sharp contrast with the strong anisotropic Hall effect of $PrTi_2Al_{20}$, the Hall effect of $LaTi_2Al_{20}$ shows rather weak anisotropy. Figures 11(c) and 11(d) show the magnetic field $B$ dependence of Hall resistivity $\rho_H$ and Hall coefficient $R_H$ of $LaTi_2Al_{20}$ for $B \parallel [111]$. The $\rho_H(B)$ shows

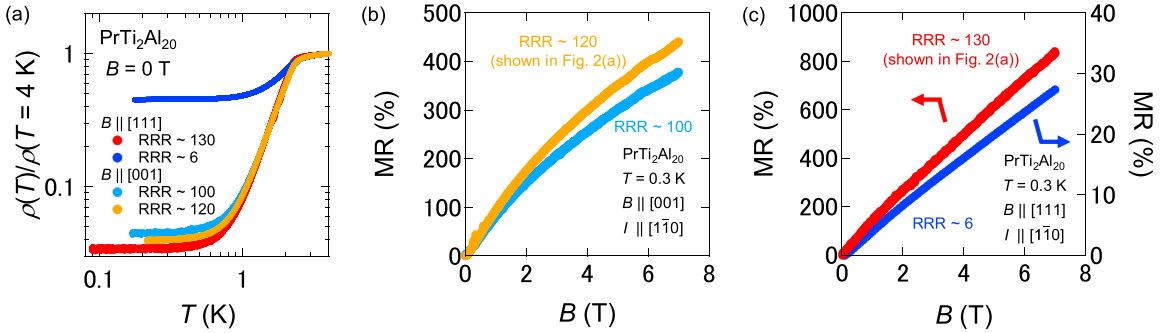


FIG. 9. RRR dependence of transport properties in $PrTi_2Al_{20}$. Temperature dependence of normalized resistivity $\rho(T)/\rho(T = 4\text{ K})$ below 4 K for various RRR samples of $PrTi_2Al_{20}$ (a). RRR dependence of MR at $T = 0.3$ K for $B \parallel [001]$ (b) and $B \parallel [111]$ (c). MR for $B \parallel [001]$ (orange) and $B \parallel [111]$ (red) are shown in Fig. 2(a) in the main text.

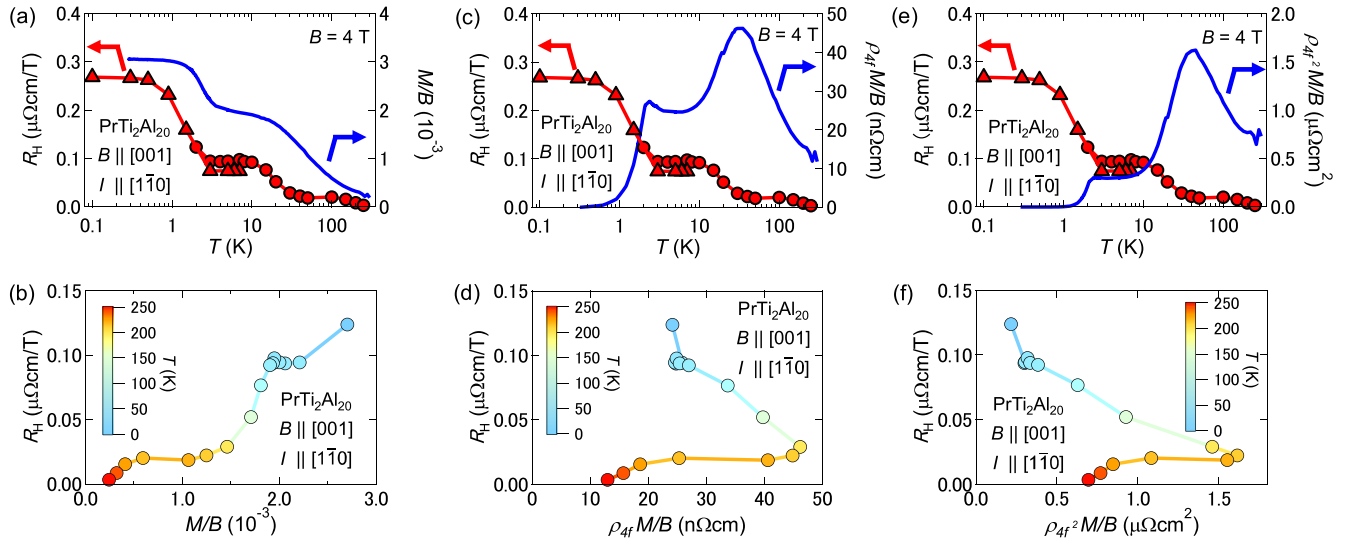


FIG. 10. Comparison of the temperature dependence of the Hall coefficient $R_H$ with $M/B$ (a), $\rho_{4f}M/B$ (c), and $\rho_{4f}^2M/B$ (e), and the scaling relations $R_{\rm H}$ vs $M/B$ (b), $R_{\rm H}$ vs $\rho_{4f}M/B$ (d), and $R_{\rm H}$ vs $\rho_{4f}^2M/B$ (f) for $PrTi_2Al_{20}$ measured at 4 T ∥ [001].

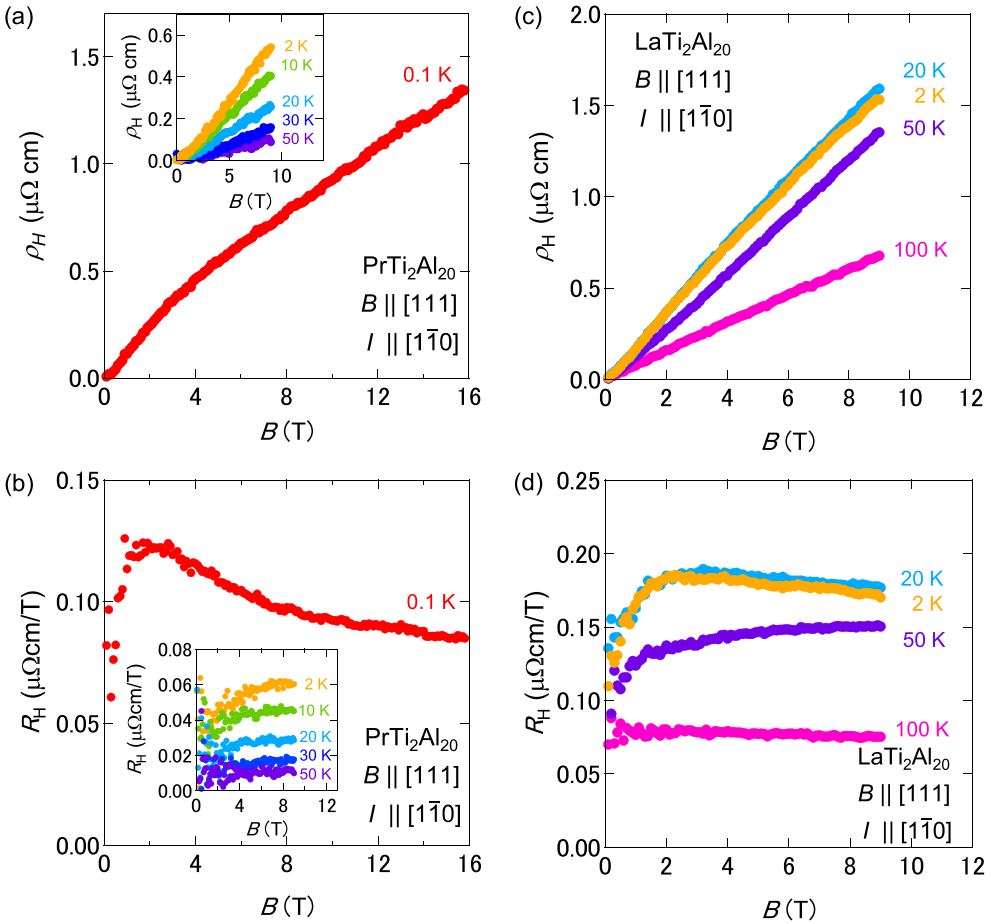


FIG. 11. (a) Magnetic field $B$ dependence of the Hall resistivity $\rho_{\rm H}$ and (b) Hall coefficient $R_{\rm H}$ of $PrTi_2Al_{20}$ for $B \parallel [111]$. The main panels of (a) and (b) show data measured at $T = 0.1$ K, and the insets show data obtained in the $T$ range 2 K $\leqslant T \leqslant$ 50 K. (c) Magnetic field $B$ dependence of the Hall resistivity $\rho_{\rm H}$ and (d) Hall coefficient $R_{\rm H}$ of $LaTi_2Al_{20}$ for $B \parallel [111]$ at 2 K $\leqslant T \leqslant$ 100 K.

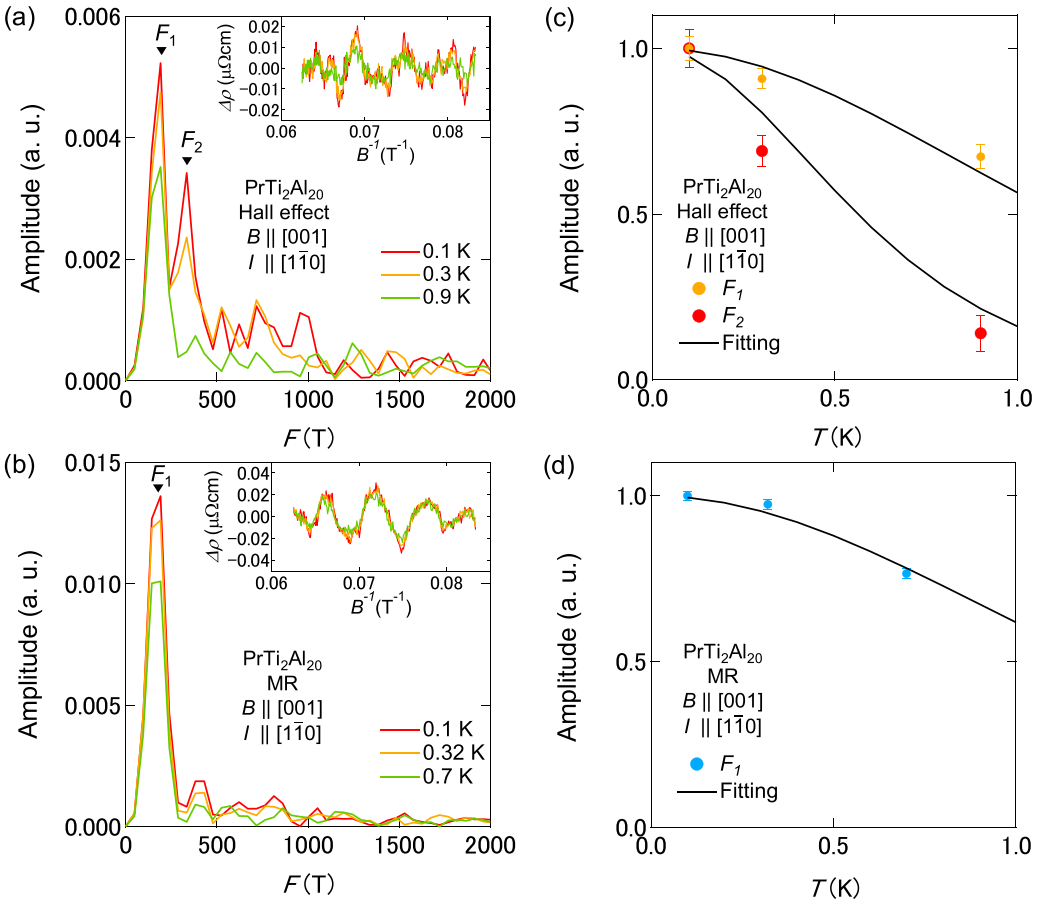


FIG. 12. (a) Fast Fourier transform (FFT) of the quantum oscillation signals observed in MR and (b) Hall effect in $PrTi_2Al_{20}$ measured under $B \parallel [001]$ at $T < 1$ K. Black arrows indicate frequencies obtained from the FFT analysis. Insets of (a) and (b) show oscillatory signals observed in Hall effect, respectively, after subtracting the polynomial fitting background from the raw data. (c) Temperature $T$ dependence of oscillatory amplitude in MR and (d) Hall effect. Solid curves indicate fits using the Lifshitz-Kosevich thermal damping term to estimate the effective mass ratio $m^*/m_0$.

nearly linear $B$ dependence for all measured $T$s, and the magnitude is similar to that observed for $B \parallel [001]$ [Fig. 4(b) and 4(d) in the main text], except for a weaker temperature dependence below 40 K.

## APPENDIX G: QUANTUM OSCILLATION IN MR AND HALL EFFECT OF $PrTi_2Al_{20}$ FOR $B \parallel [001]$

Figure 12 shows the quantum oscillation signals detected in the Hall effect and MR in $PrTi_2Al_{20}$ at $T < 1$ K and under $B \parallel [001]$. The fast Fourier Transform (FFT) analysis for the field range of 12 to 16 T reveals two frequencies, $F_1 \sim 190$ T and $F_2 \sim 330$ T, in the Hall effect [Fig. 12(a), main panel] and only $F_1$ in the MR [Fig. 12(b), main panel]. The insets of Fig. 12(a) and 12(b) show the quantum oscillation signals as a function of $1/B$ after subtracting a smooth polynomial fitting background.

Figures 12(c) and 12(d) show the temperature dependence of the oscillation amplitude in Hall effect and MR, respectively. The solid lines are fits to the Lifshitz-Kosevich thermal damping term, $X/\sinh X$, with $X = 4\pi^2 k_B m^* T/eB$ ($k_B$ is the Boltzmann constant and $e$ is the electron charge), which yields the effective mass ratio $m^*$ for each frequency. The resulting effective mass ratios are $m^*/m_0 \sim 1.6$ for $F_1$ and ~3.4 for $F_2$. Comparing with the previous DFT calculation and dHvA measurement results [27], we assign $F_1$ to the small hole-type FS pocket ($\epsilon$ branch) and $F_2$ to the $E$ branch. Our results are roughly consistent with the previous study.

## APPENDIX H: TWO-BAND ANALYSIS

We obtained the electron and hole carrier densities and mobilities from the two-band model given by the following formula [50]:

$$\rho_{\mathrm{H}}(B) = \frac{R_{\mathrm{H}}(0) + R_{\mathrm{H}}(\infty)(\mu B)^2}{1 + (\mu B)^2} B, \tag{H1}$$

$$\rho_{xx}(B) = \frac{\rho_e \rho_h (\rho_e + \rho_h) + \left(\rho_e R_h^2 + \rho_h R_e^2\right) B^2}{(\rho_e + \rho_h)^2 + (R_e + R_h)^2 B^2}, \tag{H2}$$

where

$$R_{\mathrm{H}}(0) = \frac{\rho_e^2 R_h + \rho_h^2 R_e}{(\rho_e + \rho_h)^2} = \frac{\mu_h^2 n_h - \mu_e^2 n_e}{e(n_e \mu_e + n_h \mu_h)^2}, \tag{H3}$$

$$R_{\mathrm{H}}(\infty) = \frac{R_e R_h}{R_e + R_h} = \frac{1}{e(n_h - n_e)} \tag{H4}$$

are the Hall coefficient at the low- and high-field limits, respectively. The $R_i$ and $\rho_i$ ($i = e, h$) represent the contributions to $R_{\rm H}$ and $\rho_{xx}$ from the electron or the hole band, and

$$\mu = \frac{R_e + R_h}{\rho_e + \rho_h} = \frac{\mu_e \mu_h (n_e - n_h)}{\mu_e n_e + \mu_h n_h} \tag{H5}$$

is the Hall mobility. We performed the two-band fit from 0 T to 9 T at all measured temperatures, with the Hall coefficient's low-field limit $R_H(0)$, high-field limit $R_{\rm H}(\infty)$, and Hall mobility $\mu$ being the free fitting parameters. The experimental zero-field resistivity value $\rho_{xx}(B = 0)$ (shown in Fig. 1 in the main text) is used as a constraint for the fit. We then obtained the hole and electron carrier densities and mobilities $n_h$, $n_e$, $\mu_h$, and $\mu_e$ from the best-fit values of $R_H(0)$, $R_{\rm H}(\infty)$ and $\mu$. The resulting carrier densities are largely consistent with those obtained from the first-principles calculation for $LaTi_2Al_{20}$, as shown in Table I. This comparison demonstrates that the two-band analysis yields reasonable estimation even though it is a very rough model for complex multiband systems like $PrTi_2Al_{20}$ and $LaTi_2Al_{20}$.


[1] M. N. Baibich, J. M. Broto, A. Fert, F. N. V. Dau, F. Petroff, P. Etienne, G. Creuzet, A. Friederich, and J. Chazelas, Giant magnetoresistance of (001)Fe/(001)Cr magnetic superlattices, Phys. Rev. Lett. **61**, 2472 (1988).

[2] G. Binasch, P. Grünberg, F. Saurenbach, and W. Zinn, Enhanced magnetoresistance in layered magnetic structures with antiferromagnetic interlayer exchange, Phys. Rev. B **39**, 4828(R) (1989).

[3] R. Niu and W. K. Zhu, Materials and possible mechanisms of extremely large magnetoresistance: A review, J. Phys.: Condens. Matter **34**, 113001 (2022).

[4] H. Takatsu, J. J. Ishikawa, S. Yonezawa, H. Yoshino, T. Shishidou, T. Oguchi, K. Murata, and Y. Maeno, Extremely large magnetoresistance in the nonmagnetic metal $PdCoO_2$, Phys. Rev. Lett. **111**, 056601 (2013).

[5] M. N. Ali, J. Xiong, S. Flynn, J. Tao, Q. D. Gibson, L. M. Schoop, T. Liang, N. Haldolaarachchige, M. Hirschberger, N. P. Ong, and R. J. Cava, Large, non-saturating magnetoresistance in $WTe_2$, Nature (London) **514**, 205 (2014).

[6] F. Tafti, Q. Gibson, S. Kushwaha, N. Haldolaarachchige, and R. Cava, Resistivity plateau and extreme magnetoresistance in LaSb, Nat. Phys. **12**, 272 (2016).

[7] C. Shekhar, A. K. Nayak, Y. Sun, M. Schmidt, M. Nicklas, I. Leermakers, U. Zeitler, Y. Skourski, J. Wosnitza, Z. Liu, Y. Chen, W. Schnelle, H. Borrmann, Y. Grin, C. Felser, and B. Yan, Extremely large magnetoresistance and ultrahigh mobility in the topological Weyl semimetal candidate NbP, Nat. Phys. **11**, 645 (2015).

[8] A. Narayanan, M. D. Watson, S. F. Blake, N. Bruyant, L. Drigo, Y. L. Chen, D. Prabhakaran, B. Yan, C. Felser, T. Kong, P. C. Canfield, and A. I. Coldea, Linear magnetoresistance caused by mobility fluctuations in $n$-doped $Cd_3As_2$, Phys. Rev. Lett. **114**, 117201 (2015).

[9] I. A. Leahy, Y.-P. Lin, P. E. Siegfried, A. C. Treglia, J. C. W. Song, R. M. Nandkishore, and M. Lee, Nonsaturating large magnetoresistance in semimetals, Proc. Natl. Acad. Sci. USA **115**, 10570 (2018).

[10] Q.-H. Yu, Y.-Y. Wang, R. Lou, P.-J. Guo, S. Xu, K. Liu, S. Wang, and T.-L. Xia, Magnetoresistance and Shubnikov-de Haas oscillation in YSb, Europhys. Lett. **119**, 17002 (2017).

[11] Y. Tokura, Critical features of colossal magnetoresistive manganites, Rep. Prog. Phys. **69**, 797 (2006).

[12] R. Fernandes, A. Chubukov, and J. Schmalian, What drives nematic order in iron-based superconductors? Nat. Phys. **10**, 97 (2014).

[13] S. Paschen and Q. Si, Quantum phases driven by strong correlations, Nat. Rev. Phys. **3**, 9 (2021).

[14] T. Onimaru and H. Kusunose, Exotic quadrupolar phenomena in non-Kramers doublet systems—The Cases of $PrT_2Zn_{20}$ ($T$ = Ir, Rh) and $PrT_2Al_{20}$ ($T$ = V, Ti)—, J. Phys. Soc. Jpn. **85**, 082002 (2016).

[15] A. S. Patri, I. Khait, and Y. B. Kim, Emergent non-Fermi-liquid phenomena in multipolar quantum impurity systems, Phys. Rev. Res. **2**, 013257 (2020).

[16] A. S. Patri and Y. B. Kim, Critical theory of non-fermi liquid fixed point in multipolar Kondo problem, Phys. Rev. X **10**, 041021 (2020).

[17] G. Sim, A. Mishra, M. J. Park, Y. B. Kim, G. Y. Cho, and S. Lee, Multipolar superconductivity in Luttinger semimetals, Phys. Rev. Res. **2**, 023416 (2020).

[18] A. Sakai and S. Nakatsuji, Kondo effects and multipolar order in the cubic $PrTr_2Al_{20}$ ($Tr$ = Ti, V), J. Phys. Soc. Jpn. **80**, 063701 (2011).

[19] M. J. Kangas, D. C. Schmitt, A. Sakai, S. Nakatsuji, and J. Y. Chan, Structure and physical properties of single crystal $PrCr_2Al_{20}$ and $CeM_2Al_{20}$ (M = V, Cr): A comparison of compounds adopting the $CeCr_2Al_{20}$ structure type, J. Solid State Chem. **196**, 274 (2012).

[20] T. J. Sato, S. Ibuka, Y. Nambu, T. Yamazaki, T. Hong, A. Sakai, and S. Nakatsuji, Ferroquadrupolar ordering in $PrTi_2Al_{20}$, Phys. Rev. B **86**, 184419 (2012).

[21] T. Taniguchi, M. Yoshida, H. Takeda, M. Takigawa, M. Tsujimoto, A. Sakai, Y. Matsumoto, and S. Nakatsuji, NMR observation of ferro-quadrupole order in $PrTi_2Al_{20}$, J. Phys. Soc. Jpn. **85**, 113703 (2016).

[22] T. Taniguchi, K. Hattori, M. Yoshida, H. Takeda, S. Nakamura, T. Sakakibara, M. Tsujimoto, A. Sakai, Y. Matsumoto, S. Nakatsuji, and M. Takigawa, Field-induced switching of ferro-quadrupole order parameter in $PrTi_2Al_{20}$, J. Phys. Soc. Jpn. **88**, 084707 (2019).

[23] A. Sakai, K. Kuga, and S. Nakatsuji, Superconductivity in the ferroquadrupolar state in the quadrupolar Kondo lattice $PrTi_2Al_{20}$, J. Phys. Soc. Jpn. **81**, 083702 (2012).

[24] M. Matsunami, M. Taguchi, A. Chainani, R. Eguchi, M. Oura, A. Sakai, S. Nakatsuji, and S. Shin, Kondo resonance in $PrTi_2Al_{20}$: Photoemission spectroscopy and single-impurity Anderson model calculations, Phys. Rev. B **84**, 193101 (2011).

[25] Y. Machida, T. Yoshida, T. Ikeura, K. Izawa, A. Nakama, R. Higashinaka, Y. Aoki, H. Sato, A. Sakai, S. Nakatsuji, N. Nagasawa, K. Matsumoto, T. Onimaru, and T. Takabatake, Anomalous enhancement of Seebeck coefficient in Pr-based

1-2-20 system with non-Kramers doublet ground states, J. Phys.: Conf. Ser. **592**, 012025 (2015).

[26] Y. Tokunaga, H. Sakai, S. Kambe, A. Sakai, S. Nakatsuji, and H. Harima, Magnetic excitations and $c$-$f$ hybridization effect in $PrTi_2Al_{20}$ and $PrV_2Al_{20}$, Phys. Rev. B **88**, 085124 (2013).

[27] T. Kubo, E. Matsuoka, H. Kotegawa, H. Tou, A. Nakamura, D. Aoki, H. Harima, and H. Sugawara, Fermi surface of the heavy-fermion superconductor $PrTi_2Al_{20}$, J. Phys. Soc. Jpn. **89**, 084704 (2020).

[28] K. Matsubayashi, T. Tanaka, A. Sakai, S. Nakatsuji, Y. Kubo, and Y. Uwatoko, Pressure-induced heavy fermion superconductivity in the nonmagnetic quadrupolar system $PrTi_2Al_{20}$, Phys. Rev. Lett. **109**, 187004 (2012).

[29] Y. Shimura, Q. Zhang, B. Zeng, D. Rhodes, R. Schönemann, M. Tsujimoto, Y. Matsumoto, A. Sakai, T. Sakakibara, K. Araki, W. Zheng, Q. Zhou, L. Balicas, and S. Nakatsuji, Giant anisotropic magnetoresistance due to purely orbital rearrangement in the quadrupolar heavy fermion superconductor $PrV_2Al_{20}$, Phys. Rev. Lett. **122**, 256601 (2019).

[30] S. Kittaka, T. Taniguchi, K. Hattori, S. Nakamura, T. Sakakibara, M. Takigawa, M. Tsujimoto, A. Sakai, Y. Matsumoto, and S. Nakatsuji, Field-orientation effect on ferroquadrupole order in $PrTi_2Al_{20}$, J. Phys. Soc. Jpn. **89**, 043701 (2020).

[31] A. Tsuruta and K. Miyake, Non-Fermi liquid and Fermi liquid in two-channel Anderson lattice model: Theory for $PrA_2Al_{20}$ ($A$ = V, Ti) and $PrIr_2Zn_{20}$, J. Phys. Soc. Jpn. **84**, 114714 (2015).

[32] H. Kusunose and T. Onimaru, Competition between quadrupole and magnetic Kondo effects in non-Kramers doublet systems, J. Phys.: Conf. Ser. **592**, 012099 (2015).

[33] H. Kusunose, Competing Kondo effects in non-Kramers doublet systems, J. Phys. Soc. Jpn. **85**, 064708 (2016).

[34] T. Liang, Q. Gibson, M. N. Ali, M. Liu, R. J. Cava, and N. P. Ong, Ultrahigh mobility and giant magnetoresistance in the Dirac semimetal $Cd_3As_2$, Nat. Mater. **14**, 280 (2015).

[35] R. Mondal, S. Sasmal, R. Kulkarni, A. Maurya, A. Nakamura, D. Aoki, H. Harima, and A. Thamizhavel, Extremely large magnetoresistance, anisotropic Hall effect, and Fermi surface topology in single-crystalline $WSi_2$, Phys. Rev. B **102**, 115158 (2020).

[36] Y.-Y. Lv, X. Li, J. Zhang, B. Pang, S.-S. Chen, L. Cao, B.-B. Zhang, D. Lin, Y. B. Chen, S.-H. Yao, J. Zhou, S.-T. Zhang, M.-H. Lu, M. Tian, and Y.-F. Chen, Mobility-controlled extremely large magnetoresistance in perfect electron-hole compensated $\alpha$-$WP_2$ crystals, Phys. Rev. B **97**, 245151 (2018).

[37] N. Kumar, C. Shekhar, M. Wang, Y. Chen, H. Borrmann, and C. Felser, Large out-of-plane and linear in-plane magnetoresistance in layered hafnium pentatelluride, Phys. Rev. B **95**, 155128 (2017).

[38] M. Koseki, Y. Nakanishi, K. Deto, G. Koseki, R. Kashiwazaki, F. Shichinomiya, M. Nakamura, M. Yoshizawa, A. Sakai, and S. Nakatsuji, Ultrasonic investigation on a cage structure compound $PrTi_2Al_{20}$, J. Phys. Soc. Jpn. **80**, SA049 (2011).

[39] B. Wu, V. Barrena, H. Suderow, and I. Guillamón, Huge linear magnetoresistance due to open orbits in $\gamma$-$PtBi_2$, Phys. Rev. Res. **2**, 022042(R) (2020).

[40] A. Hasegawa and H. Yamagami, Effect of the spin-orbit interaction on the Fermi surface of $LaSn_3$, J. Phys. Soc. Jpn. **60**, 1654 (1991).

[41] I. Umehara, N. Nagai, and Y. Ōnuki, High field magnetoresistance and de Haas-van Alphen effect in $LaSn_3$, J. Phys. Soc. Jpn. **60**, 1294 (1991).

[42] A. B. Pippard, *Magnetoresistance in Metals*, Vol. 2 (Cambridge University Press, Cambridge, 1989).

[43] S. Zhang, Q. Wu, Y. Liu, and O. V. Yazyev, Magnetoresistance from Fermi surface topology, Phys. Rev. B **99**, 035142 (2019).

[44] D. M. Ginsberg, *Physical Properties of High Temperature Superconductors I* (World Scientific, Singapore, 1998).

[45] S. Kasahara, T. Shibauchi, K. Hashimoto, K. Ikada, S. Tonegawa, R. Okazaki, H. Shishido, H. Ikeda, H. Takeya, K. Hirata, T. Terashima, and Y. Matsuda, Evolution from non-Fermi-to Fermi-liquid transport via isovalent doping in $BaFe_2(As_{1-x}P_x)_2$ superconductors, Phys. Rev. B **81**, 184519 (2010).

[46] S. Lee, S. Trebst, Y. B. Kim, and A. Paramekanti, Landau theory of multipolar orders in $Pr(Y)_2X_{20}$ Kondo materials ($Y$= Ti, V, Rh, Ir; $X$= Al, Zn), Phys. Rev. B **98**, 134447 (2018).

[47] F. Freyer, S. Lee, Y. B. Kim, S. Trebst, and A. Paramekanti, Thermal and field-induced transitions in ferroquadrupolar Kondo systems, Phys. Rev. Res. **2**, 033176 (2020).

[48] Y. Shimura, Y. Ohta, T. Sakakibara, A. Sakai, and S. Nakatsuji, Evidence of a high-field phase in $PrV_2Al_{20}$ in a [100] magnetic field, J. Phys. Soc. Jpn. **82**, 043705 (2013).

[49] A. Fert and P. M. Levy, Theory of the Hall effect in heavy-fermion compounds, Phys. Rev. B **36**, 1907 (1987).

[50] R. G. Chambers, The two-band effect in conduction, Proc. Phys. Soc. A **65**, 903 (1952).